Journal of Materials Chemistry C

ROYAL SOCIETY OF CHEMISTRY

PAPER

Published on 29 September 2026
Licensed under CC-BY 4.0

Check for updates

Cite this: DOI: 10.1039/d6tc01652a

Soluble pentacenes that adopt rubrene-like crystal packing

Karl J. Thorley, *[a] Gehan S. Rupasinghe,[ab] Jacob A. Coffey,[ab] Paula Alarcon Espejo,[a] Sean R. Parkin,[c] Sanjay Dutta,[c] Alexandra F. Paterson[ab] and John E. Anthony[ac]

Received 21st May 2026,
Accepted 28th September 2026

DOI: 10.1039/d6tc01652a

rsc.li/materials-c

Two of the major players in small molecule organic semiconductors are rubrene and TIPS-pentacene. Rubrene-based single-crystal transistors have achieved much higher charge mobilities than thin-film TIPS-pentacene devices, but TIPS-pentacene has the advantage of being solution processable allowing for cheap large area deposition of active layers by printing techniques. In this work we have adapted the chemical structure of TIPS-pentacene in the synthesis of new derivatives that adopt crystal packing similar to rubrene, but retain the solubility characteristics of TIPS-pentacene. We report on three such derivatives, analyzing the molecular features that affect the crystal packing, and fabricate transistor devices using solution processing techniques. We achieve hole mobilities up to 0.8 $cm^2\ V^{-1}\ s^{-1}$, improving on attempts to solution process rubrene itself.

Introduction

Rubrene is a benchmark small-molecule organic p-type semiconductor, with reliable single-crystal hole mobilities μ_H = 10 $cm^2\ V^{-1}\ s^{-1}$ at room temperature and 45 $cm^2\ V^{-1}\ s^{-1}$ at 100 K.[1] Another mainstay in the field of organic electronics is TIPS-pentacene,[2,3] which is readily solution processable and has achieved hole mobilities of 1–2 $cm^2\ V^{-1}\ s^{-1}$ in spin-coated[4] or blade-coated[5] transistor devices. The ability of both materials to operate as semiconductors in transistor devices relies on the intermolecular interactions between adjacent molecules in the solid-state (poly)crystalline environment.[6] Charges are transported through the bulk material by virtue of the overlap of frontier molecular orbitals on adjacent molecules, forming a network of interconnected orbitals determined by the molecule's specific crystal packing. The slight misalignment of the molecular orbitals can disrupt this network and influence the charge transport ability of the solid.[6]

Rubrene and TIPS-pentacene adopt very different molecular packing motifs in their respective crystalline states. Rubrene forms three different polymorphs,[7] with those from solution being inferior for charge transport compared to the desirable orthorhombic polymorph[8] from vapor growth. This crystal structure consists of a large areal overlap through a tetracene stacking interaction which provides large hole transfer integrals $t_H > 0.1$ eV. The flanking phenyl groups inhibit any edge-on interactions that are the major intermolecular solid-state interactions in unfunctionalized acenes.[9] Instead the phenyl groups direct the tetracene stacking with minimal short-axis offset, whilst also forming insulating barriers between stacks that offer well-defined layers for optimal crystal growth. Similar crystal packing arrangements have been achieved by methylthiolation of acenes,[10] which disrupts the edge-on interactions while stabilizing nose-to-face and backbone stacking interactions,[11] where single-crystal transistor devices obtained typical mobilities of 0.3 $cm^2\ V^{-1}\ s^{-1}$ with a single derivative reaching 4 $cm^2\ V^{-1}\ s^{-1}$. Attempts to solution process rubrene in transistor device fabrication have yielded low charge mobilities of 10^{-4} $cm^2\ V^{-1}\ s^{-1}$,[12] while the use of rubrene/polymer blends has increased mobility of solution-processed devices up to 0.7 $cm^2\ V^{-1}\ s^{-1}$.[7,13]

TIPS-pentacene forms a solid-state structure where all pentacene cores are parallel with one another, forming a two-dimensional brickwork motif offering multiple directions for charge transport through pentacene stacking interactions. The TIPS solubilizing groups block any edge-to-edge pentacene interactions and, similar to rubrene, form a layered barrier between the main stacking channels, allowing an ideal surface for further crystal growth. Adjusting the size of alkylsilyl groups affects the pentacene alignment within the brickwork motif, or changes the packing to 1-dimensional slip-stacked or other motifs,[3] but rarely with the nose-to-face alignment; the only example is tetramethylated TMTES-PN,[14] which has two known polymorphs, one of which is rubrene-like.[15] The same alkylsilyl

[a] Center for Applied Energy Research, University of Kentucky, Lexington 40511, KY, USA. E-mail: karl.thorley@uky.edu
[b] Department of Chemical and Materials Engineering, University of Kentucky, Lexington 40506, KY, USA
[c] Department of Chemistry, University of Kentucky, Lexington 40506, KY, USA

functionalization has been applied to other acenes besides pentacene to yield transistor devices with mobilities > 1 cm^2 V^{-1} s^{-1}.[16] All of these silylethynyl acenes possess high solubility in a range of organic solvents allowing solution processing or printing of devices.[17]

We recently reported on TIPS-pentacene derivatives containing additional phenyl groups[18] designed to limit molecular vibrations of the ethynyl bending mode. A key observation was that these derivatives possessed non-planar acene geometries, caused by the steric encumbrance between the newly installed phenyl groups and the TIPS solubilizing groups. This contortion is reminiscent of rubrene, which has a core twist of around 30° in gas-phase computed structures.[19] Functionalized rubrenes become planarized when they pack in a similar manner to the parent molecule with the characteristic nose-to-face pitched interactions, but remain contorted when adopting other types of crystal packing.[20] This encouraged us to explore whether these sterically distorted silylethynyl pentacene derivatives might be able to adopt the characteristic nose-to-face packing of rubrene while retaining the solution processing advantages of **TIPS-PN**.

In this work we report on the synthesis of these derivatives, analysis of their experimental X-ray crystal structures, computational analysis to determine the key features that allow the molecules to pack in such a way, and transistors fabricated using solution processing (Fig. 1).

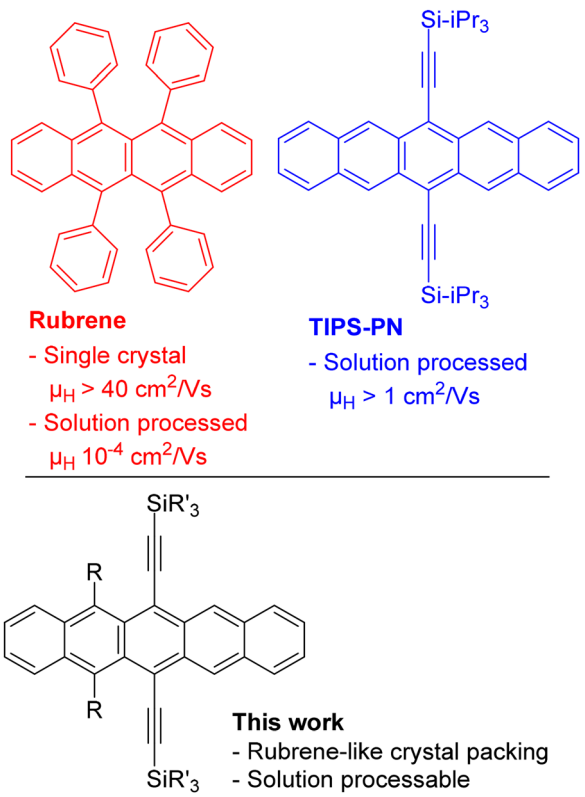


Fig. 1 Chemical structures of rubrene, **TIPS-PN**, and the general structure of materials studied in this work.

Synthesis

New pentacene materials were synthesized according to the general route that we recently reported that allowed the facile installation of different solubilizing chains and different damper groups onto a pentacene core.[18] The trimethylsilylethynyl derivative of our previously reported phenyl-pentacenes followed the exact synthetic route. For other damper groups, we found that Grignard addition with heating[21] was more efficient than using organolithium reagents. Still, the addition of thienyl Grignard to quinizarin was low yielding, and an alternative route starting with 1,4-dimethoxy-9,10-anthraquinone[22] was developed (Scheme S1). Addition of Grignard to this quinone required fewer equivalents than adding to quinizarin, and yielded a diol that could be aromatized using tin(II) chloride. Attempts to deprotect the methoxy groups with boron tribromide were low yielding, and instead it was found that direct oxidation to the 1,4-anthraquinone using cerium ammonium nitrate proceeded in quantitative yield. The synthesis of the pentacenes could follow the previously reported route; namely the reduction of 1,4-anthraquinone with sodium hydrosulfite, aldol condensation with phthalaldehyde, and addition of solubilizing trialkylsilylethynyl groups and subsequent aromatization. For alkyl Grignards, the first step did not proceed well using the adapted route, potentially due to the formation of quinodimethanes[23,24] under the tin(II) chloride de-oxygenation conditions. Therefore our preferred route to 9,10-dialkyl-1,4-anthraquinone was the direct addition of excess Grignard to quinizarin and dehydration under acidic conditions (Scheme S2).

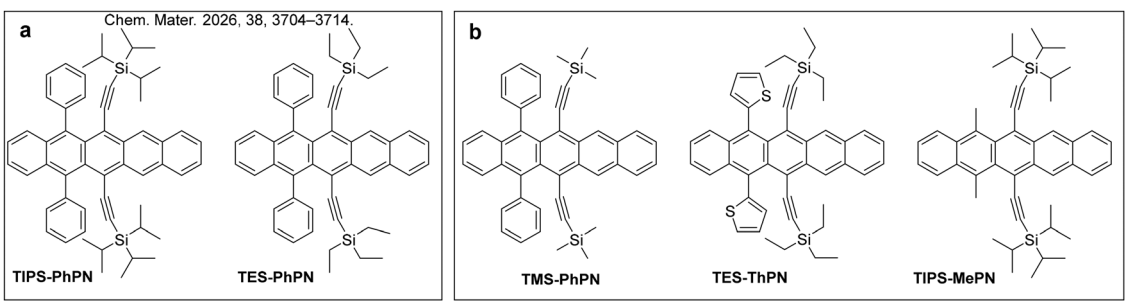


Fig. 2 Chemical structures of (a) previously reported **TIPS-PhPN** and **TES-PhPN**, and (b) the three derivatives at the focus of this work.

This journal is © The Royal Society of Chemistry 2026

Table 1 Opto-electronic data for **TMS-PhPN**, **TES-ThPN**, and **TIPS-MePN**

	λ_{max}[a]/ nm	λ_{em}[a]/ nm	Stokes shift[a]/nm	HWHM[a]/ cm^{-1}	E_{HOMO}[b]/ eV	E_{LUMO}[b]/ eV
TMS-PhPN	673	711	38	794	−5.08	−3.30
TES-ThPN	680	772	92	1752	−5.04	−3.32
TIPS-MePN	689	754	65	1251	−5.09	−3.35

[a] Absorption and emission measured in CH_2Cl_2 at 298 K. [b] Cyclic voltammetry measured in 0.1 M Bu_4N PF_6 in CH_2Cl_2 with ferrocene as internal standard. Estimated from Fc HOMO = −4.8 eV.

The synthetic routes allow the synthesis of a wide range of functionalized acenes, in this work we will focus our investigation on the three pentacene derivatives in Fig. 2b.

The solution UV-vis absorption spectra of the three molecules (Fig. S24) show similar S_0–S_1 transitions, with a shift in absorption maxima of only 16 nm across the series (Table 1). There is a noticeable difference in absorption bandwidth, with **TMS-PhPN** possessing the sharpest peaks and **TES-ThPN** the broadest. This was quantified by measuring the half-width at half-maximum (HWHM, Table 1) at the low energy (long wavelength) side of absorption band. Emission is generally weak and featureless, with no noticeable vibronic features. Stokes shifts are smallest for **TMS-PhPN** (38 nm) and largest for **TES-ThPN** (92 nm). The intensity of the emission (Fig. S24) is strongest for **TMS-PhPN** and weakest for **TES-ThPN**, pointing to **TMS-PhPN** having the smallest geometric reorganization in both the ground and excited states, while the functional group changes in **TES-ThPN** lead to greater variance in molecular geometry through the twisting of the pentacene core and interactions between the side chains. The shifts in absorption maxima are related to a combination of electronic (resonance and induction) of the additional damper groups, the twisting of the acene core, and the bending of the alkynyl triple bonds.[25] Cyclic voltammograms of each material show reversible oxidation and reduction waves within the solvent window (Fig. S21–S23) and estimated HOMO/LUMO energies (using Ferrocene internal standard) are similar across the series (Table 1). Density functional theory (DFT) computed excitation energies (tuned ωB97XD/6-31G*, Table S6) follow the trend of the experimental data. However, **TES-ThPN** is predicted to have higher ionization potential and electron affinity (lower HOMO and LUMO) by nearly 0.1 eV compared to the other materials. This discrepancy may come from the calculation of properties of a static system with fixed geometry, whereas these materials are highly flexible structures that can adopt a variety of geometries in experimental measurements. There are no noticeable differences in the distribution of the frontier orbitals across the molecules in the DFT calculations (Fig. S29–S32).

Crystal packing

In our previous work,[18] we found that **TIPS-PhPN** and **TES-PhPN** were able to form crystal packing motifs with substantial pentacene overlap despite their contorted acene cores and additional side-group steric interactions. **TES-PhPN** adopted a 1-dimensional stacking structure, where solubilizing chains interdigitated between stacks. **TIPS-PhPN** formed crystals with a broadly 2-dimensional brickwork pattern, except that one of the interactions was displaced along the pentacene short axis, limiting acene–acene electronic interaction in that direction. Both materials possessed a contorted acene core in the crystals, similar to the handful of rubrene derivatives where the packing deviates from the parent rubrene.[20]

By adjusting the size of the solubilizing alkylsilyl chains and the neighboring group that induces the strained system, we found that the derivatives depicted in Fig. 2b adopted packing motifs reminiscent of rubrene (Fig. 3). Views along all crystallographic axes are provided in Fig. S26–S28 for comparison. The crystal structures all feature 1-dimensional stacks with large areas of overlap between adjacent aromatic cores, a nose-to-face herringbone interaction that may also contribute to charge transport, and cleavage planes between adjacent stacks which should allow for more uniform film formation from solution when compared to materials with interdigitating side chains. Despite exhibiting twisted minimum energy structures in DFT calculations, the acene cores of **TMS-PhPN**, **TES-ThPN** and Me-**TIPS-PN** are generally flat due to packing forces. Side groups bend above or below the acene plane to relieve the intramolecular steric stress, rather than inducing the twists observed in **TIPS-PhPN** and **TES-PhPN**. Transfer integrals, t_H, were computed for molecular pairs in the rubrene-like crystal structures (Fig. 3), where coupling in the stacking direction is comparable to rubrene with t_H between 70 and 128 meV. These couplings are larger than those for **TIPS-PN** (30 meV) suggesting that in idealized systems the rubrene packing should offer higher charge mobility. Nose-to-face interactions offer smaller coupling values of < 20 meV, which can contribute to charge

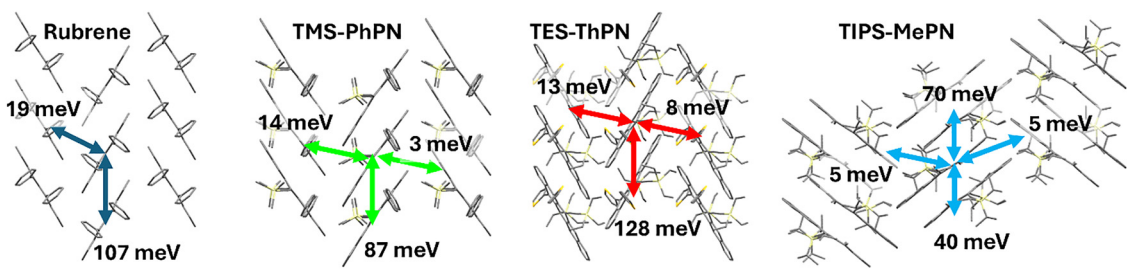


Fig. 3 Crystal packing and computed (PBE0/6-31G*) electronic coupling in Rubrene, **TMS-PhPN**, **TES-PhPN** and **TIPS-MePN** crystals.

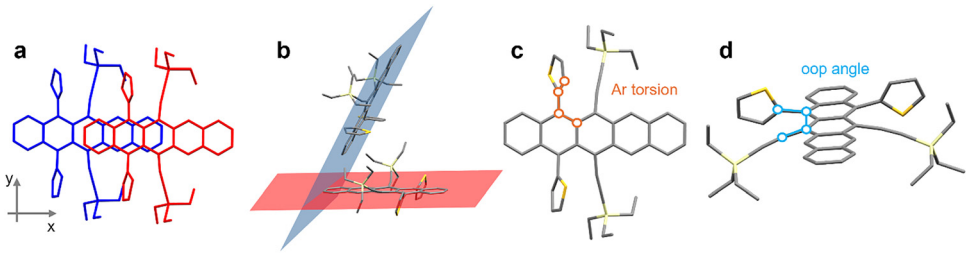


Fig. 4 Definitions of (a) molecular axes (*x*, long-axis and *y*, short-axis) used to discuss molecular solid-state packing, (b) nose-to-face angle defined between molecular planes, (c) aryl torsional angle and (d) out-of-plane distortion.

transport, but the majority of charge transport should be through the more strongly coupled acene face-to-face stacks.

In the case of **TIPS-MePN** there is a "pairing up" effect that consists of two asymmetrically aligned molecules that form a repeating ensemble along the main stacking direction. This gives rise to two different transfer integrals within the main acene stacks. In **TMS-PhPN** and **TES-ThPN** there is a molecular ordering consisting of the phenyl or thienyl end of one molecule overlapping with the unsubstituted end of the neighbouring pentacene which results in the transfer integrals being identical throughout the stack. In previously reported 2D **TIPS-PhPN** and 1D **TES-PhPN** the molecular interactions alternated between the phenyl ends overlapping, or the non-phenyl ends overlapping. Thus it appears that the way that the molecules align with one another within the initial acene stacks strongly influences the final crystal packing.

To further discuss molecular alignments in the crystals, Fig. 4 defines different directions and angles used in the following discussion. The *x*- and *y*-directions are defined as the pentacene long- and short-axes as shown in Fig. 4a. The nose-to-face angles were determined by the angle between the two pentacene planes in Fig. 4b. The aryl torsional dihedral is formed from four sequential carbon atoms over the thiophene or phenyl rings and the pentacene core, while an out-of-plane dihedral angle between the alkyne and neighbouring group is used to describe the deviation of the pentacene from planarity.

The first columns of Table S5 shows how molecules in the stacking pairs of each crystal structure align with one another. Notably, the pentacenes exhibiting rubrene-like packing have x-displacements on the order of 6 Å or less, compared to the 8 Å in 1D slip-stack **TES-PhPN**. The y-displacement is also small for the rubrene-packing pentacenes ($<$ 0.6 Å) and larger for 1D-stacked **TES-PhPN** (1–2 Å). Stacking distances are typical at around 3.5 Å, except for one contact in **TES-PhPN** with *z*-displacement of 3.1 Å, although the distance between overlapping portions of the molecules is larger than this value derived from molecular centres. The nose-to-face herringbone interaction is comparable in the pentacenes that possess this interaction, with **TES-ThPN** the most similar to rubrene itself (61°), and **TMS-PhPN** and **TIPS-MePN** adopting a more orthogonal interaction. While this intermolecular angle can influence the electronic coupling between adjacent molecules, this coupling is also dependent on displacements in the *x*- and *y*-directions,[26] and so it is not straightforward to determine whether changes in coupling are due to this nose-to-face angle itself.

On a single molecule scale, the aryl torsion and out-of-plane angles between the aryl and ethynyl groups were also directly measured from the X-ray structures. In comparison to the 1D-stacked **TES-PhPN** that has an aryl torsion of 58°, **TMS-PhPN** and **TES-ThPN** have a more orthogonal aryl ring (66 and 72° respectively) that approaches that of rubrene (77°) with less conjugation between pentacene and aryl ring. The out-of-plane angles are quite similar across the class of materials, with angles ranging from 20 to 25°, while the twisted core of **TES-PhPN** is larger at 32°.

Periodic DFT and theoretical crystal motifs

To establish requirements for rubrene-like packing, we focused on the **TMS-PhPN**, **TES-PhPN**, and **TES-ThPN** series due to the similarities in their molecular structures. **TES-PhPN** adopts a 1D stacked structure, but reducing the size of the trialkylsilyl groups allows the rubrene packing. This can also be achieved by swapping phenyl groups of **TES-PhPN** for thiophenes in **TES-ThPN**. Starting from the experimental crystal structures for each material, we performed plane-wave periodic DFT calculations to optimize the unit cell structure, while also allowing the unit cell to adapt its parameters. Upon finding optimized structures, we then modified the chemical structure (*e.g.* swapping TES for TMS groups, or phenyl for thiophene) to create hypothetical 1D-stacked and rubrene-like structures for each molecule.

The unit cell parameters of the relaxed solid-state structures are presented in Table S7. The structures where the "correct" molecule is present show a general expansion of the unit cell compared to experimental X-ray structures obtained at low temperature. Unit cell parameters are similar when **TES-PhPN** and **TES-ThPN** are exchanged, given that most of the space-filling is taken up by the roughly same size of solubilizing alkylsilyl groups. Adopting **TMS-PhPN** into the **TES-PhPN** or **TES-ThPN** crystal packing results in greater changes to the unit cell parameters, although the reduced unit cell volume results in comparable densities. Computed unit cell binding energies of **TMS-PhPN** are quite similar across three different crystal packings (-200 to -208 kJ mol^{-1}), while **TES-ThPN** has similar binding energies in its own rubrene-like packing (-244 kJ mol^{-1}) and the theoretical 1D arrangement (-247 kJ mol^{-1}). However **TES-PhPN** is more stable in its experimentally observed 1D stack structure than the rubrene-like packing (-244 *vs.* -227 kJ mol^{-1}).

This journal is © The Royal Society of Chemistry 2026

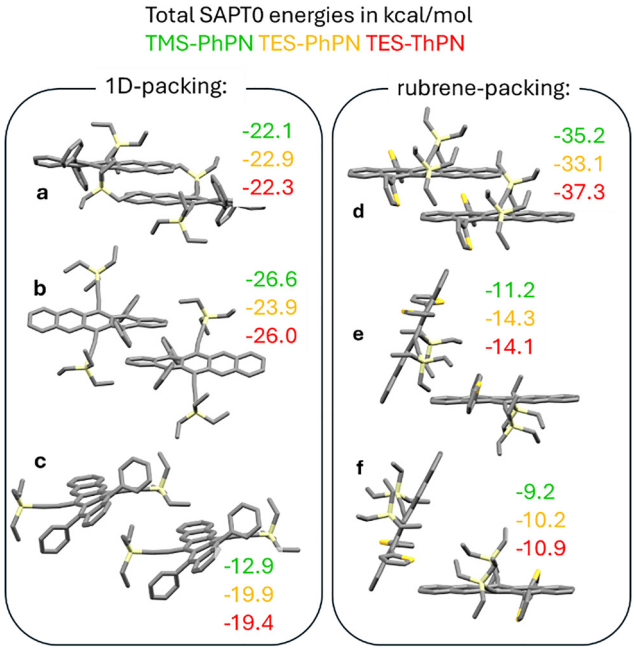


Fig. 5 Select molecular pairs from DFT-optimized unit cells in 1D slip-stack packing (a–c, left) and rubrene-like packing (d–f, right), and the total SAPT0/jun-cc-PVDZ energies in kcal mol^{-1} for each of **TMS-PhPN** (green), **TES-PhPN** (yellow), and **TES-ThPN** (red) in each molecular pair.

We next used symmetry adapted perturbation theory (SAPT0) to look at pairwise interaction energies from each of the DFT-optimized unit cells, where Fig. S33 shows the total SAPT energies *versus* the intermolecular center-of-molecule (COM) distances. The 1D packing originating from **TES-PhPN** shows distinct groups of dimers, with the directly interacting stacked molecules possessing SAPT energies of −20 to −30 kcal mol^{-1} and COM separations of 8–10 Å. The dimer where the unsubstituted ends of the pentacenes interact (Fig. 5a) shows little difference in SAPT0 energy between the three different pentacene derivatives, while the dimer where the thienyl/phenyl groups interact (Fig. 5b) in **TES-PhPN** is weaker by 2 kcal mol^{-1} compared to the other two materials. At separations of between 10 and 14 Å there are a host of interactions that result from the interdigitation of alkylsilyl or aryl side chains interacting with neighboring pentacene surfaces. The closest of these at 10 Å (Fig. 5c) has much stronger non-covalent interactions than the others due to silyl groups of both pentacenes being involved in this dispersion stabilized packing motif. The SAPT energy for **TMS-PhPN** is much smaller than the two TES- derivatives due to the smaller size and weaker dispersion stabilization of the TMS group. Molecular pairs with separation $>$ 14 Å are between adjacent stacks and offer further small stabilization energies.

In contrast, there are more well-defined groups in the rubrene-like packing (Fig. S33) which originates from the **TES-ThPN** X-ray structure. Clusters of molecular pairs with large separation $>$ 16 Å and low interaction energy $<$ 5 kcal mol^{-1} come from interactions between molecular stacks. The nose-to-face interactions lie in the 9–10 Å COM range with moderate SAPT energies of −10 to −15 kcal mol^{-1}. There are two distinct molecular pairs of this type, with the one that has the interaction of the silyl group with the face of the aryl neighbor (Fig. 5e) being slightly more stabilizing than the one where the edge of the aryl group is involved (Fig. 5f). The change in thienyl/phenyl groups does not change these energies much, while the smaller TMS group offers slightly less stabilization than TES groups. The direct acene-stacking interactions with COM distances of around 7 Å have much higher binding energy due to their closer packing. Changing from phenyl to thiophene groups results in a 4 kcal mol^{-1} stabilization of **TES-ThPN** over **TES-PhPN**, with **TMS-PhPN** laying intermediate between the two. SAPT energies between these closely packed molecular pairs appears to present the largest discrepancy between molecules, and the most likely culprit for the change in crystal packing.

In both 1d- and rubrene-like packing, **TMS-PhPN** shows shorter *x*-displacements and larger *y*-displacements in the acene-stacking interactions compared to **TES-PhPN** or **TES-ThPN**, a consequence of the smaller alkylsilyl chains needing to get close enough together to interact. The stacking interactions of **TES-PhPN** in rubrene-packing is larger (3.94 Å) than in the other two pentacenes (3.8 Å) due to the generally increased side group size. The slightly greater stacking distance results in less stabilizing dispersion interaction (E_{DISP} for **TES-ThPN** = −52 kcal mol^{-1} *versus* **TES-PhPN** E_{DISP} = −47 kcal mol^{-1}, Fig. S34). While there is also less exchange repulsion from the greater stacking distance in **TES-PhPN**, there is also less electrostatic stabilization which originates from charge penetration through the π-electron cloud.[27] The differences in exchange and electrostatics largely cancel each other out, leaving the greater dispersion stabilization as the deciding factor in non-covalent binding energy.

From this computational study it appears that to obtain rubrene-like packing the acene must have substituents that can fill space close to the acene edge and encourage stacking interaction with small short-axis displacement. Next the solubilizing groups must be small enough to allow the acene stacking with large areal overlap and small stacking distance to gain as much stabilization from dispersion and electrostatic charge penetration. This appears to be the limiting factor keeping **TES-PhPN** from adopting rubrene-like packing due to increased sidegroup size forcing a larger stacking distance and weaker non-covalent interaction. From this key dimer, further stacking interactions and nose-to-face interactions can grow into layers of the expanded crystalline structure.

Organic thin film transistors

To probe the effect of crystal packing on solid-state charge transport, we fabricated transistors in bottom-contact top-gate architecture as outlined in the supporting information. The active layers were deposited from 10 mg mL^{-1} tetralin solutions of either neat pentacene derivative or pentacene derivative:poly-triarylamine (PTAA) blends by spin-coating, and Cytop dielectric spin coated on top. First, **TES-ThPN** devices showed the lowest hole mobilities, out of the three derivatives tested. Specifically, **TES-ThPN** devices with channel length (L) = 80 μm had maximum

hole mobilities of 0.025 $cm^2 V^{-1} s^{-1}$, and average mobility of 0.021 $cm^2 V^{-1} s^{-1}$ (Table 2). While **TES-ThPN** has the lowest mobility out of the derivatives, these numbers indicate excellent reproducibility across 10 devices with L = 80 μm, and the mobility is already a two orders of magnitude increase over solution processed rubrene devices.[12] Next, we used PTAA as a polymer binder, to control crystallization through phase separation during solvent evaporation and film formation.[28–31] Table 2 shows that **TES-ThPN**:PTAA blends have increased mobility across all channel lengths (Fig. S49), with an average mobility of 0.049 $cm^2 V^{-1} s^{-1}$ for devices with L = 40 μm.

Higher mobilities were observed in transistors made with **TIPS-MePN** as the semiconductor layer, compared to **TES-ThPN**. Here, neat **TIPS-MePN** devices have a mobility of 0.17 $cm^2 V^{-1} s^{-1}$ at L = 100 μm, and an average mobility of 0.13 $cm^2 V^{-1} s^{-1}$. **TIPS-MePN**:PTAA blends showed similar hole mobilities, at a marginally higher maximum of 0.21 $cm^2 V^{-1} s^{-1}$. Of note is that both neat and blend **TIPS-MePN** transistors have excellent device-to-device variation across 25 transistors with 5 different channel lengths (30, 40, 50, 80 and 100 μm): For neat **TIPS-MePN**, the devices had an average of 0.10 $cm^2 V^{-1} s^{-1}$ and standard deviation 0.03 $cm^2 V^{-1} s^{-1}$, whereas the **TIPS-MePN**:PTAA blends had an average mobility of 0.12 $cm^2 V^{-1} s^{-1}$ and standard deviation 0.06 $cm^2 V^{-1} s^{-1}$.

Finally, mobility was enhanced even further in transistors made with the third derivative, **TMS-PhPN**, which have excellent maximum mobilities of 0.70 $cm^2 V^{-1} s^{-1}$ and 0.85 $cm^2 V^{-1} s^{-1}$, respectively, for neat **TMS-PhPN** and **TMS-PhPN**:PTAA blends. These **TMS-PhPN** hole mobilities are comparable to efforts to solution process rubrene with additives,[13] or polymer binders,[7] with maximum values of 0.70 $cm^2 V^{-1} s^{-1}$. It is important that neat **TMS-PhPN** developed in this work achieves the same hole mobilities without additives, because this simplifies the solution processing method, and is therefore compatible with low-cost processing associated with organic electronics. Average mobilities at optimal channel lengths (L = 100 μm) were 0.49 $cm^2 V^{-1} s^{-1}$ for neat **TMS-PhPN**, and 0.63 $cm^2 V^{-1} s^{-1}$ for **TMS-PhPN**:PTAA blends (L = 80 μm). We note that high mobilities were measured when all channel lengths were taken into account. Namely, the average mobilities were 0.37 $cm^2 V^{-1} s^{-1}$ and 0.33 $cm^2 V^{-1} s^{-1}$, respectively, for neat **TMS-PhPN** and **TMS-PhPN**:PTAA blends. The latter observation of higher average mobilities is because the mobility values were more consistent across 25 transistors (Fig. S51). As well as outperforming other solution processed rubrene devices, the mobilities of **TMS-PhPN** devices are around double that of the previously reported **TIPS-PhPN**,[18] which has a roughly 2D-brickwork packing, and achieved average and peak mobilities of 0.36 and 0.42 $cm^2 V^{-1} s^{-1}$, respectively, at optimal channel lengths, and when a polymer binder was used (Fig. 6).

Each of the three pentacenes with rubrene-like packing reported in this work far exceed the transistor hole mobilities of solution-processed rubrene, and are comparable to rubrene devices employing additives or polymer binders to encourage crystalline film growth. For the three pentacenes discussed here, only a slight increase in mobility was observed when PTAA was used as a polymer binder. Notably, the high mobilities achieved from the neat materials prove that the inclusion of alkylsilyl solubilizing chains into materials that can achieve the rubrene-like packing, can enhance the solution processability, for cheaper large area deposition relevant to real-world organic electronic applications. In general, there is only a small variation in mobility with channel length, which indicates that the transistors are not significantly impacted by contact effects. The trend in device mobilities is opposite to that expected from computed transfer integrals (Fig. 4), which would have predicted that **TES-ThPN** should show highest mobilities. This highlights the importance of processibility and film formation in achieving high mobilities in organic thin-film transistors.

To investigate the thin-film microstructures compared to the single crystal packing, grazing-incidence wide-angle X-ray scattering measurements were performed on the small molecules spin-coated onto single-crystal silicon wafers. 2D GIWAXS patterns, together with 1D linecuts and azimuthal intensity integrations, are provided in Fig. S52–S54. The 2D GIWAXS pattern of **TES-ThPN**, which crystallizes in the monoclinic Pc space group, exhibits broad lamellar scattering with an approximately isotropic distribution, indicating the presence of crystalline domains with a broad range of orientations. The out-of-plane (q_z) linecut reveals the (100) and (200) lamellar reflections at q_z = 0.36 $Å^{-1}$ and 0.72 $Å^{-1}$, respectively. The corresponding $d_{(100)}$ spacing of approximately 17.45 Å is consistent with the single crystal value calculated from a sin β = 16.49 Å. The in-plane (q_{xy}) linecut additionally shows a broad, low intensity feature near $q_{xy} \approx 0.99$ $Å^{-1}$ ($d \approx 6.37$ Å), which is consistent with diffraction from the (010) planes and compares reasonably with the single crystal $d_{(010)}$ spacing of 6.95 Å. The broad, continuous azimuthal intensity distribution further supports significant orientational disorder within the film.

On the other hand, **TMS-PhPN** shows a more pronounced preferred orientation, with both edge-on and face-on crystallites. The azimuthal intensity profiles display face-on features at $\Psi \approx 0^\circ$ and 180° alongside stronger edge-on peaks at $\Psi \approx 80^\circ$ and 100° (with 90° cut off by the beamstop). The out-of-plane linecut shows a (100) reflection at $q_z \approx 0.21$ $Å^{-1}$, followed by the

Table 2 Average and maximum hole mobilities (μ_H) at best operating channel lengths (L) in organic thin-film transistors made from spin coated pentacene derivatives or PTAA/pentacene derivative blends

	Neat			1 : 1 PTAA blend		
	L/μm	$\mu_{(ave)}$/$cm^2 V^{-1} s^{-1}$	$\mu_{(max)}$/$cm^2 V^{-1} s^{-1}$	L/μm	$\mu_{(ave)}$/$cm^2 V^{-1} s^{-1}$	$\mu_{(max)}$/$cm^2 V^{-1} s^{-1}$
TES-ThPN	80	0.021	0.025	40	0.049	0.057
TMS-PhPN	100	0.49	0.70	80	0.63	0.85
TIPS-MePN	80	0.13	0.17	80	0.14	0.21

 This journal is © The Royal Society of Chemistry 2026

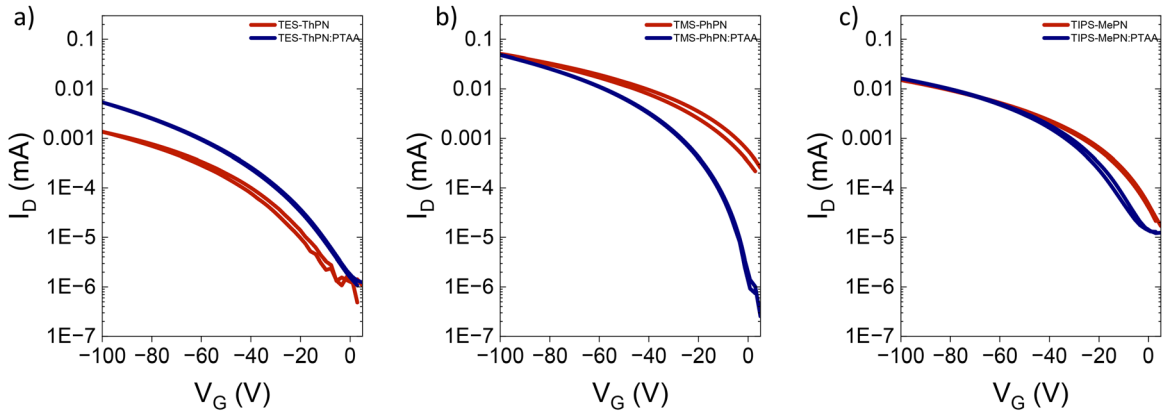


Fig. 6 Transfer characteristics measured in the saturation regime for the best-performing devices listed in Table 2, comparing neat and 1 : 1 PTAA blend devices of (a) **TES-ThPN**, (b) **TMS-PhPN**, and (c) **TIPS-MePN**.

(200) reflection at $q_z \approx 0.41$ Å^{-1}. The $d_{(100)}$ spacing of 29.92 Å obtained from GIWAXS closely matches the theoretical interplanar spacing ($d_{(100)}$ = 30.20 Å) calculated for the monoclinic $P2/c$ space group. Notably, the (100) reflection is observed in the thin-film GIWAXS pattern despite having negligible intensity in the single crystal simulation ($F_{100} \approx 0$). This suggests a deviation from the ideal crystal structure, potentially arising from interfacial symmetry breaking, local structural distortion, or altered molecular packing. In addition, in-plane scattering at $q_{xy} \approx 0.41$ Å^{-1} corresponds to a d-spacing comparable to that of the (200) reflection and is consistent with the presence of face-on crystallites. An additional in-plane feature at $q_{xy} \approx 0.97$ Å ($d \approx 6.35$ Å) agrees well with the (010) spacing along the b-axis (b = 6.45 Å). Together, out-of-plane lamellar reflections and in-plane π–π stacking indicate a predominantly edge-on molecular orientation with a fraction of face-on crystallites.

Lastly, **TIPS-MePN** exhibits a distinct orientation distribution compared with **TMS-PhPN**, with the principal diffraction features occurring at off-axis azimuthal angles rather than being concentrated along the principal in-plane or out-of-plane directions. The azimuthal intensity profiles show sharp diffraction features centered near $\Psi \approx 20^\circ$ and 160°, indicating a preferentially tilted orientation of the crystalline domains relative to the substrate. The out-of-plane linecut displays the (100) reflection at $q_z \approx 0.18$ Å^{-1} ($d \approx 34.91$ Å), followed by the (200) reflection at $q_z \approx 0.35$ Å^{-1}, in good agreement with the single-crystal $d_{(100)}$ spacing of 34.36 Å calculated for the monoclinic $P2_1/c$ structure. Similar to **TMS-PhPN**, the observation of the (100) reflection in the thin film, despite its absent intensity in the idealized single-crystal pattern, may indicate changes in molecular packing or local symmetry at the thin-film interface. In addition, the (010) is not observed, consistent with (0k0) reflections with odd k values being forbidden due to the 2_1 screw axis along the b-axis in the $P2_1/c$ space group.

The observed structural differences can be correlated with charge carrier mobility. **TMS-PhPN** exhibits the highest mobility, consistent with the pronounced molecular ordering and predominantly edge-on orientation, which favors efficient in-plane charge transport through the π-stacked backbone. **TIPS-MePN** also displays well-defined crystalline order, but its tilted molecular orientation may result in less direct alignment of the transport pathways with the substrate plane. Lastly, **TES-ThPN** exhibits a broad, nearly isotropic scattering distribution, indicative of greater orientational disorder. This reduced structural order can disrupt efficient intermolecular charge-transport pathways, potentially contributing to increased charge localization, and, consequently, lower mobility.

Conclusions

Following on from our previous work on contorted pentacenes that had gas-phase geometries reminiscent of high-performance small molecule semiconductor rubrene, we have adapted the molecular structure to obtain three examples that adopt the iconic nose-to-face herringbone packing of rubrene crystals. The inclusion of trialkylsilyl side chains endow the pentacenes presented here with greater solubility than rubrene that allows for solution deposition processes in the fabrication of transistor devices. We have analysed the crystal packing of the pentacenes through computational unit-cell simulations to determine non-covalent interactions that most impact the ability of these materials to adopt the rubrene-like packing as opposed to previously reported 1-D slipped stack, despite very small changes in molecular structure. Organic thin film transistors fabricated using spin-coating show an increase in hole mobility by 3 orders of magnitude, from 10^{-4} cm^2 V^{-1} s^{-1} for rubrene,[12] to average mobilities of 0.1 cm^2 V^{-1} s^{-1} for **TIPS-MePN** and 0.49 cm^2 V^{-1} s^{-1} for **TMS-PhPN**. Deposition as a polymer blend further increased the charge carrier mobility to an average of 0.63 cm^2 V^{-1} s^{-1} for 1 : 1 **TMS-PhPN**/PTAA. Maximum mobilities for **TMS-PhPN** as a neat material (0.70 cm^2 V^{-1} s^{-1}) and polymer blend (0.85 cm^2 V^{-1} s^{-1}) rival maximum reported mobilities of similar devices using rubrene/polymer blends.[7,21] Through an increased understanding of non-covalent interactions in rubrene-like packing, refinement of more soluble materials could further improve charge mobilities in solution processed transistors.

Conflicts of interest

There are no conflicts to declare.

Data availability

The data supporting this article have been included as part of the supplementary information (SI). Supplementary information is available. See DOI: https://doi.org/10.1039/d6tc01652a.

CCDC 2555944, 2555945 and 2555947 contain the supplementary crystallographic data for this paper.[32a–c]

Acknowledgements

K. J. T. and J. E. A. thank the U.S. National Science Foundation, Division of Materials Research (DMR-2414541) for supporting the development of new organic semiconductors. S. R., J. A. C, and A. F. P. thank the Defense Advanced Research Projects Agency (DARPA) for financial support through grant number D24AP00298-00, and the National Science Foundation through grant numbers 2441261 and 2349830. We thank Michela Martinelli and Nico Briot at the University of Kentucky for assistance in thin film X-ray diffraction measurements.

References

1 W. Xie, K. A. McGarry, F. Liu, Y. Wu, P. P. Ruden, C. J. Douglas and C. D. Frisbie, *J. Phys. Chem. C*, 2013, **117**, 11522–11529.
2 J. E. Anthony, J. S. Brooks, D. L. Eaton and S. R. Parkin, *J. Am. Chem. Soc.*, 2001, **123**, 9482–9483.
3 J. E. Anthony, D. L. Eaton and S. R. Parkin, *Org. Lett.*, 2002, **4**, 15–18.
4 S. K. Park, T. N. Jackson, J. E. Anthony and D. A. Mourey, *Appl. Phys. Lett.*, 2007, **91**, 063514.
5 G. Giri, S. Park, M. Vosgueritchian, M. M. Shulaker and Z. Bao, *Adv. Mater.*, 2014, **26**, 487–493.
6 V. Coropceanu, J. Cornil, D. A. da Silva Filho, Y. Olivier, R. Silbey and J.-L. Brédas, *Chem. Rev.*, 2007, **107**, 926–952.
7 P. S. Jo, D. T. Duong, J. Park, R. Sinclair and A. Salleo, *Chem. Mater.*, 2015, **27**, 3979–3987.
8 O. D. Jurchescu, A. Meetsma and T. T. M. Palstra, *Acta Crystallogr., Sect. B*, 2006, **62**, 330–334.
9 C. C. Mattheus, A. B. Dros, J. Baas, A. Meetsma, J. L. D. Boer and T. T. M. Palstra, *Acta Crystallogr., Sect. C*, 2001, **57**, 939–941.
10 K. Kanazawa, K. Bulgarevich, K. Kawabata and K. Takimiya, *Cryst. Growth Des.*, 2023, **23**, 5941–5949.
11 C. Wang, D. Hashizume, M. Nakano, T. Ogaki, H. Takenaka, K. Kawabata and K. Takimiya, *Chem. Sci.*, 2020, **11**, 1573–1580.
12 X. Gao, W. Liu, H. Liu, M. Huang, S. He, M. Zhang, Z. Hua and C. Zhu, *Sci. Rep.*, 2020, **10**, 12183.
13 N. Stingelin-Stutzmann, E. Smits, H. Wondergem, C. Tanase, P. Blom, P. Smith and D. de Leeuw, *Nat. Mater.*, 2005, **4**, 601–606.
14 G. R. Llorente, M.-B. Dufourg-Madec, D. J. Crouch, R. G. Pritchard, S. Ogier and S. G. Yeates, *Chem. Commun.*, 2009, 3059–3061.
15 S. Illig, A. S. Eggeman, A. Troisi, L. Jiang, C. Warwick, M. Nikolka, G. Schweicher, S. G. Yeates, Y. Henri Geerts, J. E. Anthony and H. Sirringhaus, *Nat. Commun.*, 2016, **7**, 10736.
16 S. Subramanian, S. K. Park, S. R. Parkin, V. Podzorov, T. N. Jackson and J. E. Anthony, *J. Am. Chem. Soc.*, 2008, **130**, 2706–2707.
17 H. T. Yi, M. M. Payne, J. E. Anthony and V. Podzorov, *Nat. Commun.*, 2012, **3**, 1259.
18 K. J. Thorley, G. S. Rupasinghe, S. Ruhunage, M. Ogbaje, V. Bhat, S. Parkin, C. Risko, A. Paterson and J. E. Anthony, *Chem. Mater.*, 2026, **38**, 3704–3714.
19 A. S. Paraskar, A. R. Reddy, A. Patra, Y. H. Wijsboom, O. Gidron, L. J. W. Shimon, G. Leitus and M. Bendikov, *Chem. – Eur. J.*, 2008, **14**, 10639–10647.
20 W. A. Ogden, S. Ghosh, M. J. Bruzek, K. A. McGarry, L. Balhorn, V. Young, Jr., L. J. Purvis, S. E. Wegwerth, Z. Zhang, N. A. Serratore, C. J. Cramer, L. Gagliardi and C. J. Douglas, *Cryst. Growth Des.*, 2017, **17**, 643–658.
21 H. Laatsch, *Liebigs Ann. Chem.*, 1986, **1986**, 839–858.
22 H. L. Newson, D. A. Wild, S. Y. Yeung, B. W. Skelton, G. R. Flematti, J. E. Allan and M. J. Piggott, *J. Org. Chem.*, 2016, **81**, 3127–3135.
23 S. C. Dickerman, J. H. Berg, J. R. Haase and R. Varma, *J. Am. Chem. Soc.*, 1967, **89**, 5457–5458.
24 H. A. Staab, W. Herbst and C. Krieger, *Chem. Ber.*, 1987, **120**, 93–95.
25 K. J. Thorley, A. Shakir, A. Kudrimoti, S. R. Parkin, S. R. Rather and J. E. Anthony, *Adv. Opt. Mater.*, 2026, e71674.
26 K. J. Thorley and C. Risko, *J. Mater. Chem. C*, 2016, **4**, 3825–3832.
27 S. M. Ryno, C. Risko and J.-L. Brédas, *Chem. Mater.*, 2016, **28**, 3990–4000.
28 T. Losi, F. A. Viola, E. Sala, M. Heeney, Q. He, H. Kleemann and M. Caironi, *Small Methods*, 2024, **8**, 2400546.
29 A. F. Paterson, N. D. Treat, W. Zhang, Z. Fei, G. Wyatt-Moon, H. Faber, G. Vourlias, P. A. Patsalas, O. Solomeshch, N. Tessler, M. Heeney and T. D. Anthopoulos, *Adv. Mater.*, 2016, **28**, 7791–7798.
30 J. Smith, W. Zhang, R. Sougrat, K. Zhao, R. Li, D. Cha, A. Amassian, M. Heeney, I. McCulloch and T. D. Anthopoulos, *Adv. Mater.*, 2012, **24**, 2441–2446.
31 R. Hamilton, J. Smith, S. Ogier, M. Heeney, J. E. Anthony, I. McCulloch, J. Veres, D. D. C. Bradley and T. D. Anthopoulos, *Adv. Mater.*, 2009, **21**, 1166–1171.
32 (*a*) CCDC 2555944: Experimental Crystal Structure Determination, 2026, DOI: 10.5517/ccdc.csd.cc2rsnt1; (*b*) CCDC 2555945: Experimental Crystal Structure Determination, 2026, DOI: 10.5517/ccdc.csd.cc2rsnv2; (*c*) CCDC 2555947: Experimental Crystal Structure Determination, 2026, DOI: 10.5517/ccdc.csd.cc2rsnx4.

 This journal is © The Royal Society of Chemistry 2026